Additive Manufacturing 21 (2018) 30–40

Contents lists available at ScienceDirect

Additive Manufacturing

journal homepage: www.elsevier.com/locate/addma

Full Length Article

Finite element analysis and experimental validation of the thermomechanical behavior in laser solid forming of Ti-6Al-4V

Xufei Lu[a,b], Xin Lin[a,b,*], Michele Chiumenti[c], Miguel Cervera[c], JunJie Li[a,b], Liang Ma[a,b], Lei Wei[a,b], Yunlong Hu[a,b], Weidong Huang[a,b]

[a] State Key Laboratory of Solidification Processing, Northwestern Polytechnical University, Youyixilu, Xi'an, Shaan Xi 710072, People's Republic of China
[b] Key Laboratory of Metal High Performance Additive Manufacturing and Innovative Design, MIIT China, Northwestern Polytechnical University, Youyixilu, Xi'an, Shaan Xi 710072, People's Republic of China
[c] International Center for Numerical Methods in Engineering (CIMNE), Universidad Politécnica de Cataluña (UPC), Edificio C1, Campus Norte, Gran Capitán s/n, 08034 Barcelona, Spain

ARTICLE INFO

Keywords:
Finite element analysis
Laser solid forming
Thermomechanical behavior
Sensitivity
Pre-heating procedures

ABSTRACT

A three-dimensional (3D) thermomechanical coupled model for Laser Solid Forming (LSF) of Ti-6Al-4V alloy has been calibrated through experiments of 40-layers metal deposition using different scanning strategies. The sensitivity analysis of the mechanical parameters shows that the thermal expansion coefficient as well as the elastic limit of Ti-6Al-4V have a great impact on the mechanical behavior. Using the validated model and optimal mechanical parameters, the evolution of thermo-mechanical fields in LSF has been analyzed. It has been found that the stresses and distortions develop in two stages, after the deposition of the first layer and during the cooling phase after the manufacturing of the component. The cooling phase is the responsible of 70% of the residual stresses and 60% of the total distortions. The analyses indicate that by controlling the initial substrate temperature (pre-heating phase) and the final cooling phase it is possible to mitigate both distortion and residual stresses. Hence, the influence of different pre-heating procedures on the mechanical fields has been analyzed. The results show that increasing the pre-heating temperature of the substrate is the most effective way to reduce the distortions and residual stresses in Additive Manufacturing.

1. Introduction

Additive Manufacturing (AM) is an advanced solid free-form manufacturing technology that allows for complex shaping with high-performance requirements. AM consists of the metal deposition of thin layers according to a specific scanning strategy, eventually forming net or near net-shape components [1]. Laser Solid Forming (LSF) [2] is one of the several AM technologies, in which the powder feeding is coaxial with the power input (laser or electron beam). Compared with traditional fabrication methods, LSF can greatly improve the material saving, reduce the processing cost, as well as reaching high mechanical performance comparable with those of forging processes. It can be used not only for the fabrication of new components but also for parts repairing. However, during the scanning sequence, the metal deposition undergoes rapid heating and cooling cycles with high temperature values and large temperature gradients which induce significant residual stresses and distortions. Hence, the geometrical accuracy and mechanical properties of the fabricated parts can be compromised. Further research regarding the formation and evolution of both distortions and residual stresses in LSF processes is mandatory to enhance this manufacturing technology.

Finite element (FE) analysis is an important tool to predict the temperature evolution, distortions and residual stresses during the AM process. The experimental work can be minimized by taking advantage of FE analyses used to optimize the process parameters and to study both the material behavior and the structural response. The AM software can be used to predict the temperature evolution [3–8], as well as the distortions and residual stresses [9–13].

Many researchers have validated their models using *in situ* experimental measurements techniques [5,11,14,15] and analyzed the residual stresses and distortions of the final products. Although many thermomechanical models have been calibrated for the AM of titanium alloys, the material properties used to characterize the material behavior of Ti-6Al-4V are very different. On the one hand, in thermal analysis the most sensitive parameters are the heat absorption and both the heat convection and heat radiation coefficients [3,7,15–19]. On the other hand, the mechanical response depends on the characterization of the constitutive model thought the definition of the corresponding

* Corresponding author at: State Key Laboratory of Solidification Processing, Northwestern Polytechnical University, Youyixilu, Xi'an, Shaan Xi 710072, People's Republic of China.
E-mail address: xlin@nwpu.edu.cn (X. Lin).

https://doi.org/10.1016/j.addma.2018.02.003
Received 12 December 2017; Received in revised form 13 February 2018; Accepted 14 February 2018
Available online 19 February 2018
2214-8604/

elastic modulus and plastic law [3,18,20–23]. Regarding these, it is very difficult to take advantage from the establishment of a common material database, particularly because there exist many differences in the definition of the constitutive laws used to characterize the mechanical behavior of the material. This problem is amplified when the mechanical response must be characterized within the entire temperature range of the AM processes, from the room temperature to and above the melting point. Moreover, the residual stresses and distortions during the metal deposition are accumulated according to the scanning sequence used for the metal deposition, which drives the local temperature evolution and temperature gradients while evolving during the AM process.

Denlinger et al. [15,18,24] developed and validated a model for the Directed Energy Deposition (DED) process. *In situ* measurements of distortion, temperature and residual stresses were used to evaluate the accuracy of their model during the DED processing of Ti-6Al-4V. They found that the transformation strains in Ti-6Al-4V reduce the stress field till vanishing for temperatures above 690 °C. The authors proposed to reset both the stress and strain fields when the temperature is above 690 °C to obtain better agreement with the experimental results. They also observed that shorter dwell times produce higher temperature values and less pronounced temperature gradients, leading to significantly lower residual stresses and distortions of the built. However, a detailed analysis of the stress formation by coupling the different thermomechanical fields during DED processes is rarely analyzed. Martina et al. [25] and Szost et al. [26] measured the residual stresses induced by Wire + Arc Additive Manufacturing (WAAM) of Ti-6Al-4V walls. The results showed that the maximum longitudinal stresses are concentrated just above the interface between the substrate and the wall and the magnitude of these stresses typically reduces from top of the wall, becoming compressive at the bottom surface. Nevertheless, the generation and development of these stress fields were not explored.

In the literature, different methods to reduce the distortions and residual stresses have been proposed taking advantage from the previous experiences in welding processes, for instance, by modifying the structural design as a function of the new AM technologies, or by controlling the process parameters, as well as by means of heat treatments to achieve this objective [27]. Chin et al. [28] and Klingbeil et al. [29] found that moderate heating of the substrate above the room temperature before DED, as well as better mechanical constraints of the substrate can mitigate both deformations and stresses. Nevertheless, the pre-heating strategies need further investigation. Cao et al. [30] found that when the laser pre-heating on the substrate is increased by electron beam free-form fabrication, the distortion firstly increases and then reduces, while the maximum residual stress gradually decreases. However, this reduction is small. Nowadays, the underlying mechanisms of mitigating distortions and residual stresses for AM processes and, particularly, for the LSF technique are not yet well understood.

In this work, a fully coupled 3D thermo-mechanical FE model is calibrated using the experimental data obtained in our Labs. Hence, a sensitivity analysis of the mechanical properties has been systematically performed to find the optimal parameters for the numerical simulation of the thermo-mechanical problem. In this way, both the temperature values and the final distortions of Ti-6Al-4V metal deposition by LSF are optimized. The structural response obtained using different material data to characterize the mechanical behavior is discussed in detail. Finally, the validated model is used to investigate the influence of different pre-heating methods and possible alternative strategies to mitigate the final distortions and the residual stresses.

2. AM process modeling

The framework used for the numerical simulation of the AM process by LSF consists of a thermo-mechanical solver for transient analysis. An automatic time-marching scheme is used to advance in time. At each time-step, a staggered solution performs the thermal and mechanical analyses, sequentially. As a result, a fully coupled solution is achieved being the mechanical problem fully dependent on the temperature field through the user defined temperature-dependent material database. Both elastic moduli and plastic flow can account for the thermal softening. Furthermore, the strain-hardening, the material creep, as well as the annealing mechanisms are taken into account to fully characterize the material behavior in the entire temperature range from room temperature to and above the melting point. Reciprocally, the thermal analysis is also coupled with the mechanical problem. The heat generated by the plastic dissipation is included as source term in the balance of energy equation. Furthermore, due to the deposition of the different layers during the building process, the heat losses by convection and radiation change because of the modification of the actual boundary conditions (external surfaces) for the thermal analysis. A detailed description of the model is given in references [11,16,22].

2.1. Transient thermal model

The transient heat transfer analysis is governed by the balance of energy equation. The local (strong) format of this equation is stated as:

$$\dot{H} = -\nabla\cdot\boldsymbol{q} + \dot{Q} + \dot{D}_{mech} \tag{1}$$

where $\dot{H}$, $\dot{Q}$ and $\dot{D}_{mech}$ represent the rates of enthalpy, heat source and thermo-mechanical dissipation (per unit of volume), respectively. The heat flux (per unit of surface) $\mathbf{q}$ is expressed as a function of the temperature gradient through Fourier's law as:

$$\mathbf{q} = -k\nabla T \tag{2}$$

where $k(T)$ is the temperature-dependent thermal conductivity.

Integrating Eq. (1) over the entire computational domain, it is possible to write the integral (weak) form of the energy balance as:

$$\int_{\Omega} (\delta\vartheta\ \dot{H})\ dV + \int_{\Omega} [\nabla(\delta\vartheta)\ k\nabla T]\ dV = \int_{\partial\Omega} \delta\vartheta\ (q_{conc} + q_{rad})\ dS \tag{3}$$

where Ω and $\partial\Omega$ are the integration domain closed by its boundary surfaces, respectively, while $\delta\vartheta$ are the test functions of the temperature field.

The heat loss by convection, q_{conv}, can be computed by means of Newton's law as:

$$q_{conv} = h_{conv}(T - T_{env}) \tag{4}$$

where h_{conv} is the temperature-dependent heat transfer coefficient (HTC) due to the convection flow, T is the temperature at the material surface, and T_{env} the temperature of the surrounding environment.

The radiation heat flux is computed using Stefan–Boltzmann's law as:

$$q_{rad} = \sigma_{rad}\varepsilon_{rad}(T^4 - T_{env}^4) \tag{5}$$

where σ_{rad} is the Stefan–Boltzmann constant and ε_{rad} is the emissivity parameter, respectively.

2.2. Mechanical model

The mechanical problem is governed by the balance of momentum equation. The local form of this equation, written for quasi-static conditions, can be stated as:

$$\nabla\cdot\boldsymbol{\sigma} + \mathbf{b} = 0 \tag{6}$$

where $\mathbf{b}$ represents the prescribed body forces (per unit of volume), $\nabla\cdot(\cdot)$ is the divergence operator and $\boldsymbol{\sigma}(\mathbf{u})$ denotes the Cauchy stress tensor as a function of the displacement field, $\mathbf{u}$.

The mechanical constitutive law can be written as:

$$\boldsymbol{\sigma} = \mathbf{C}\colon \varepsilon_{\mathrm{e}} \tag{7}$$

where the elastic strains, ε_{e}, are computed as:

$$\varepsilon_e = \varepsilon - \varepsilon_p - \varepsilon_T \quad (8)$$

as a function of the total strain tensor ε, the plastic strains ε_p and the thermal deformations ε_T, respectively. **C** is the fourth order elastic stiffness tensor. A detailed description of the thermal shrinkage as well as the visco-plastic flow including strain-hardening, thermal softening and creep behavior can be found in references [11,22]. The effect of stress relaxation due to phase transformation has been included into the model following the method by Denlinger et al. [18]. The optimum stress relaxation temperature has been set to 690 °C [15]. When the temperature exceeds this value, an instantaneous annealing is applied as well as a gradual reduction of the yield surface vanishing once the melting point is reached.

2.3. FE analysis

The coupled thermomechanical analyses are performed using *Comet*, a FE software developed at the International Center for Numerical Methods in Engineering (CIMNE) [31]. The three-dimensional modeling, the FE mesh generation and the result post-processing are all performed using the GiD pre-post-processor [32].

Fig. 1 shows the FE mesh used for the model calibration through experiments, as well as the mid yz cross-section used to plot many of the results of this work. The mesh contains 19,614 Q1P0 hexahedral 8-noded elements and 25,468 nodes. Q1P0 hexahedral elements are chosen because they yield more accurate results than standard tetrahedral elements in case of isochoric plastic flow [33–37], as well as to represent the incompressible behavior of the purely viscous material behavior above the melting point [22]. According to the mesh convergence study in references [16,18,21] and considering the computational capabilities available, the FE mesh consists of three elements to represents the laser spot size and one element through the layer thickness. A sensitivity analysis to check the performance of the chosen FE mesh has been carried out taking into account the work presented in [16] as well as the discussion in references [18,20]. The mesh is coarsened far from the Heat Affected Zone (HAZ), ensuring the required accuracy and saving computational-time. The element dimension is $1 \times 1 \times 0.15\,\text{mm}^3$. The heat source moves element-by-element according to the scanning sequence, that is, 0.15 mm at each time-step. Hence, optimal time-integration accuracy is preserved.

In the LSF process the part is gradually built at each time step according to the metal-deposition process. In the numerical simulation, the birth-dead-elements technique is employed [11,16,22]. Hence, before starting the cladding process, all the elements belonging to the AM built are inactive. According to the deposition sequence, at each time step the elements belonging to the new metal deposition layer are activated using an octree-based searching algorithm.

The laser beam in LSF follows a continuous path. However, using a time-step $\Delta t = t^{n+1} - t^n$ in the discrete problem, the melting pool moves along the scanning path jumping from time t^n to time t^{n+1}. Hence, the searching algorithm activates all the elements belonging to the volume affected by the power source in-between the initial and final positions of the melt-pool within this interval; this is referred to as the Heat Affected Volume (HAV):

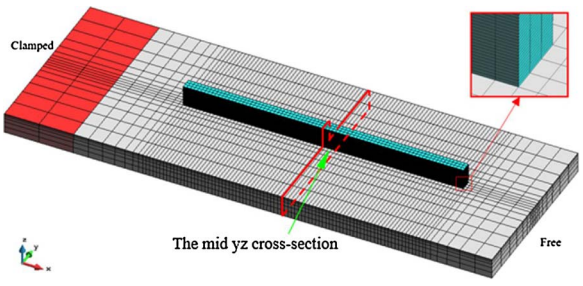

Fig. 1. FE mesh used for the numerical simulation of the AM process.

Table 1
Temperature-dependent material properties of Ti-6Al-4V.

Temperature (°C)	Density (kg/m^3)	Thermal Conductivity (W/(m °C))	Heat Capacity (J/(kg °C))	Poisson's Ratio
20	4420	7	546	0.345
500	4350	12.6	651	0.37
995	4282	22.7	753	0.43
1100	4267	19.3	641	0.43
1200	4252	21	660	0.43
1600	4198	25.8	732	0.43
1700	3886	83.5	831	0.43
1800	3818	83.5	831	0.43

$$V_{pool}^{\Delta t} = \sum_{e=1}^{n_e} V^{(e)}\Big|_{e \varepsilon HAV} \quad (9)$$

The (average) density distribution of the heat source (per unit of volume) is computed as:

$$\dot{Q} = \frac{\eta_p \dot{P}}{V_{pool}^{\Delta t}} \quad (10)$$

where $\dot{P}$ is the total energy input introduced by the laser and η_p is the heat absorption parameter (efficiency). Reference [16] details the modeling hypotheses for the power distribution inside the melting pool.

2.4. Material properties of Ti-6Al-4V

The temperature-dependent thermal and mechanical properties of Ti-6Al-4V used in the analysis for both the substrate and the cladding are shown in Table 1 and Fig. 2, respectively. The thermal properties of Ti-6Al-4V, such as density, specific heat and thermal conductivity are very similar to those found in literature. Observe that when the temperature exceeds the melting point, the heat conductivity is increased to take into account the heat convection flow inside the melting pool. The mechanical properties responsible of both the elastic behavior and the plastic flow are obtained from references [18,20–22,38]. The sensitivity of the different mechanical properties shown in Fig. 2 on the numerical results will be discussed in the following sections.

2.5. Boundary conditions

The plate is clamped as a cantilever at the upper and lower surfaces as shown in Fig. 1. Both convection and radiation conditions are considered in all external surfaces. The emissivity of Ti-6Al-4V is 0.1 for LSF, while the convective heat transfer coefficient used in the simulation is presented in Table 2. Moreover, heat conduction at the contact interface between the plate and the clamping system is considered to account for the thermal inertia of the supporting structure. By correlating simulated and experimental results, the heat transfer coefficient used for Newton's model is set to 50 [W/m^2 °C]. The power absorption efficiency, η is 0.13. The ambient temperature is 25 °C. For all the simulations, the cooling time is 5000 s to ensure that the part cools down to room temperature.

3. Experimental setting

3.1. Experimental method

Two samples of Ti-6Al-4V are fabricated using the LSF process on a Ti-6Al-4V titanium alloy substrate with the dimensions $140 \times 50 \times 6\,\text{mm}^3$. Plasma Rotating Electrode Processed (PREPed) Ti-6Al-4V powder with the diameters between 44 μm and 149 μm is used for the metal deposition. The powder is dried in a vacuum oven at 150 °C for 3 h before the LSF processing. Each substrate is burnished by

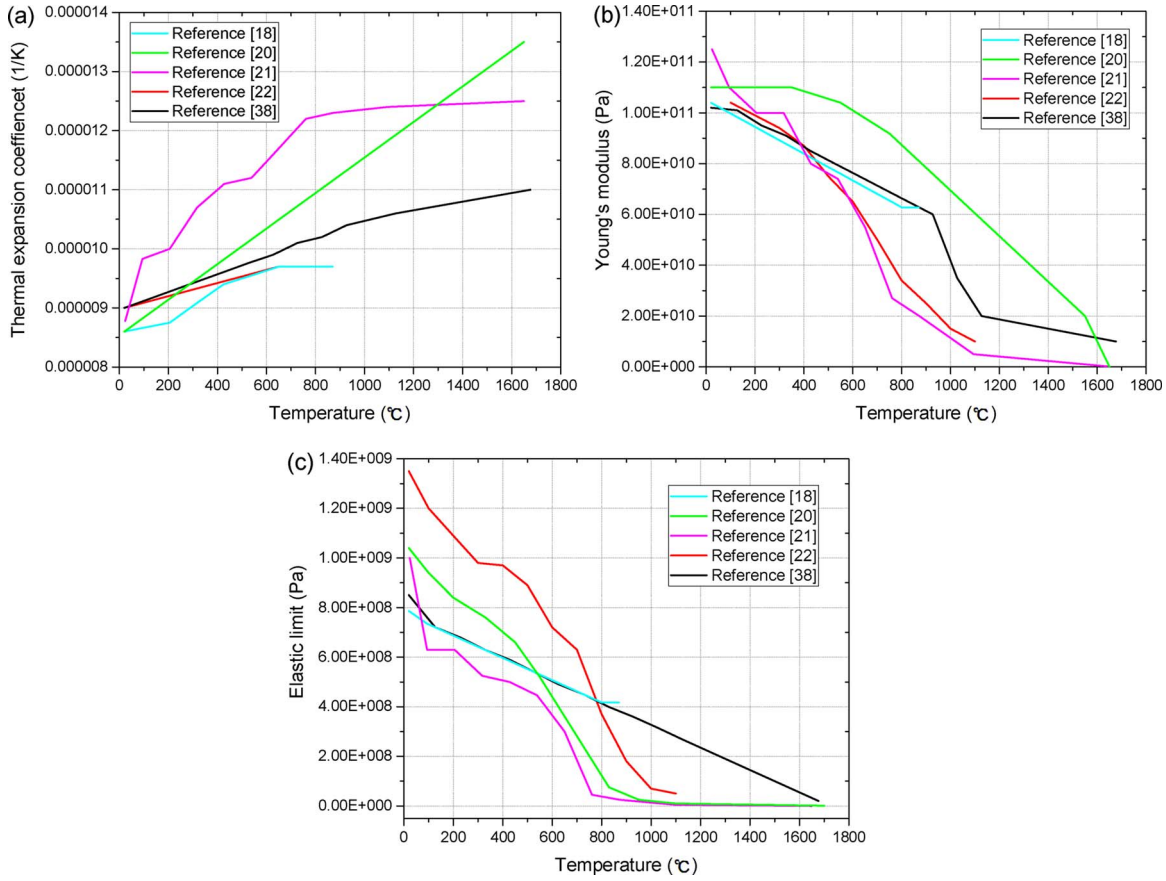

Fig. 2. Ti-6Al-4V titanium alloy: mechanical properties.

Table 2
The convection heat transfer coefficient used in the simulation.

Temperature (°C)	20	1000	2000
Deposit (W/(m^2 °C))	6	10	15
Substrate (W/(m^2 °C))	6	8	10

Table 3
Processing parameters of LSF.

Case	Spot diameter (mm)	Laser power (kW)	Scanning speed (mm/s)	Return speed (mm/s)	Up-lift height (mm)	Scanning strategy
1	3	2	10	10	0.15	Reciprocating
2	3	2	10	50	0.15	Unidirectional

sand paper and cleaned using acetone prior to LSF. The metal deposition consists of 40 layers with dimensions of 6 mm high, 80 mm long and 3 mm wide. Fig. 3(a) shows the LSF–IIIB system using a CO_2-laser source with a maximum power input of 4 kW in a close chamber filled with argon to prevent oxidation during the laser cladding. The laser beam has a diameter of 3 mm and the laser output mode presents a bimodal distribution. Fig. 3(b) shows the coaxial nozzles used for the powder feeding. The feeding rate is set to 5 g/min. Two different scanning strategies, reciprocating and unidirectional, are adopted. The process parameters are shown in Table 3.

3.2. *In situ* measurement of distortion and temperature

In order to perform *in situ* measurements of the distortion during the deposition process, the substrate is clamped on one end to a supporting

Fig. 3. Laser solid forming system:(a) LSF–IIIB device; (b) Powder feeding nozzles.

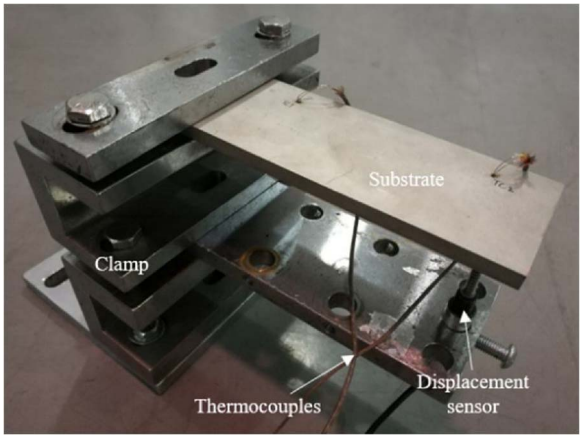

Fig. 4. Experimental setup to measure the distortion and temperature of the substrate during the AM process.

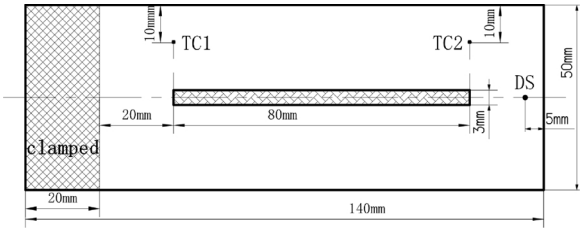

Fig. 5. Sample dimensions and location of the thermocouples.

structure (not simulated), allowing for free deflection at the opposite side during the entire LSF process and the following cooling phase, as shown in Fig. 4. *In situ* deflection measurements are taken with a WXXY PM11-R1-20L Displacement Sensor (DS) placed below the bottom edge at the free side of the plate. This DS has a measurement range of 20 mm and a linear accuracy of 0.02%. Temperature is measured at different locations on the top of the substrate using 2 Omega GG-K-30 type K thermocouples with a measurement uncertainty of 2.2 °C. The distortion and the thermocouple signals are acquired using a Graphtec GL-900 8 high-speed data-logger. Fig. 5 shows the locations of the two thermocouples and the DS on the substrate.

4. Results and discussion

4.1. Sensitivity analysis to mechanical properties

The calculated distortion and the longitudinal residual stress distribution refer to the mid yz cross-section along the transversal direction. According to the scanning strategy for Case 1 (see Table 3), different analyses have been performed using the mechanical properties of Ti-6Al-4V obtained from the following references [18,20–22,38]. The corresponding results are shown in Fig. 6. It can be seen from Fig. 6(a) that, when using the parameters from references [20] and [21], the simulated results of the LSF process are in close agreement with the experimental measurements. In particular, the simulation results using the material parameters from reference [21] also show good agreement with the experimental measurements in the final cooling phase. Contrarily, the distortion calculated using the parameters from reference [20] is significantly smaller than the actual measurements. Observe that the distortion of the substrate calculated using the parameters from references [18,22,38] presents a large deviation from the experimental evidence (e.g. using the parameters from reference [22] the final distortion is only half of the experimental evidence). Fig. 6(b) shows that the residual stress distributions obtained using the material data from references [20,21] are very similar. The maximum residual tensile stresses are located in the HAZ, 1 mm below the top surface of the substrate. The residual stresses obtained using material parameters from references [21] and from reference [20] are smaller. Observe that the results obtained using parameters from references [18,22,38] exhibit a great stress gradient at the interface between the substrate and the metal deposition This result is not consistent with the usual trend for the longitudinal residual stress as reported in [18,30,39–42]. Hence, the numerical simulation performed adopting the material data from reference [21] is the most accurate and can be used to characterize the mechanical behavior of the manufacturing process using the LSF technology.

Fig. 7 shows the sensitivity to the thermal expansion coefficient, the Young's modulus and the elastic limit, keeping as a reference the results obtained adopting the material data from [21]. It can be seen that the thermal expansion coefficient largely affects the prediction for the overall distortion and residual stresses. The larger is the thermal expansion coefficient, the greater are the plate distortion and the residual stresses. Moreover, the effect of the Young's modulus on the final distortion is mainly induced by the final cooling phase. Nevertheless, the Young's modulus has only a moderate global effect. Finally, the effect due to the value of the elastic limit on the simulated results is very clear: the calculations performed with a too high elastic limit cannot correctly characterize the history of both distortion and residual stress distribution because they are not able to capture the actual plastic flow.

The existing material databases used to characterize Ti-6Al-4V behavior are mostly derived by testing samples obtained by traditional manufacturing processes such as casting and metal forming. One of the main conclusion of this work is that the values so obtained are not suitable for the LSF characterization and it is necessary to establish accurate material properties to characterize the material behavior for this kind of material processing.

4.2. Temperature evolution

Fig. 8 shows the temperature evolution obtained from numerical simulations and experimental measurements at the thermocouple locations TC1 and TC2 of the substrate shown in Fig. 5. The agreement is notable. During the LSF process, the substrate is firstly heated-up by the laser from room temperature to the pre-heating temperature. As a result, an initial rapid heating of the substrate is observed in Fig. 8. Later, the building process is performed through a sequence of 40 deposited layers. During the heating phase, the temperature at the thermocouples continues to increase even when the heat loss becomes higher than the energy input. Both experimental and numerical curves show several peaks due to regular movement of the laser heat source to deposit the different layers. When the deposition is completed, the accumulated heat is gradually dissipated and the substrate gradually cools down. Observe that the peak temperature recorded at TC1 is about 50 °C lower than values at TC2, since TC1 is closer to the HAZ than TC2. There are some differences between the simulation and the experimental plots which may be due to a lack of accuracy when modeling both heat radiation and heat convection mechanisms. One possible reason for this is the gas flow inside the process chamber used to prevent oxidation during LSF process.

The average error during the entire simulation registered for Case 1 and Case 2 is calculated as:

$$\%Error = \frac{100 \sum_{i=1}^{n} \left| \frac{(x_{exp})_i - (x_{sim})_i}{(x_{exp})_i} \right|}{n} \tag{11}$$

where n is the number of simulation time increments, i is the current time increment, x_{exp} is the experimental value, and x_{sim} is the corresponding simulation value. Table 4 shows the average error at TC1 and TC2 for Case 1 and Case 2: the maximum error using the selected thermal parameters is less than 5.21%.

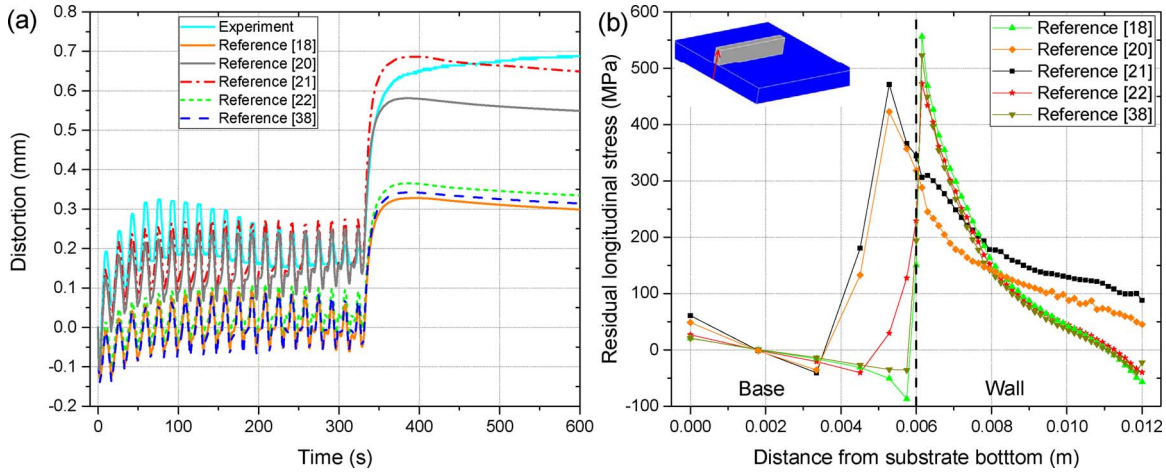

Fig. 6. The effect of different Ti-6Al-4V mechanical properties on the calculation results: (a) Distortion, (b) Residual stress.

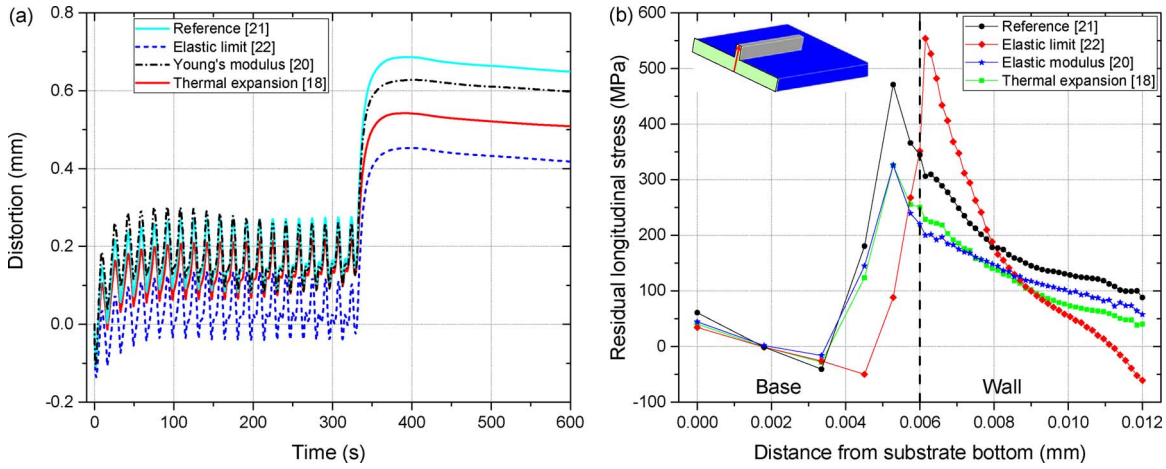

Fig. 7. Sensitivity to the thermal expansion coeffiencient and the elastic limit: (a) Distortion, (b) Residual stresses.

4.3. Distortion evolution

Fig. 9 compares the evolution of the vertical displacement at the position of the DS on the substrate obtained by simulation and the experimental measurement when using two different scanning methods: Case 1 and Case 2, respectively. The evolution of the distortion of the substrate in Case 1 can be split in 4 phases. During the deposition of the 1st layer, the thermal expansion of the upper part of the

Table 4
The average error of the temperature evolution.

Case	% Error TC1	% Error TC2
1	2.36	5.06
2	5.21	3.73

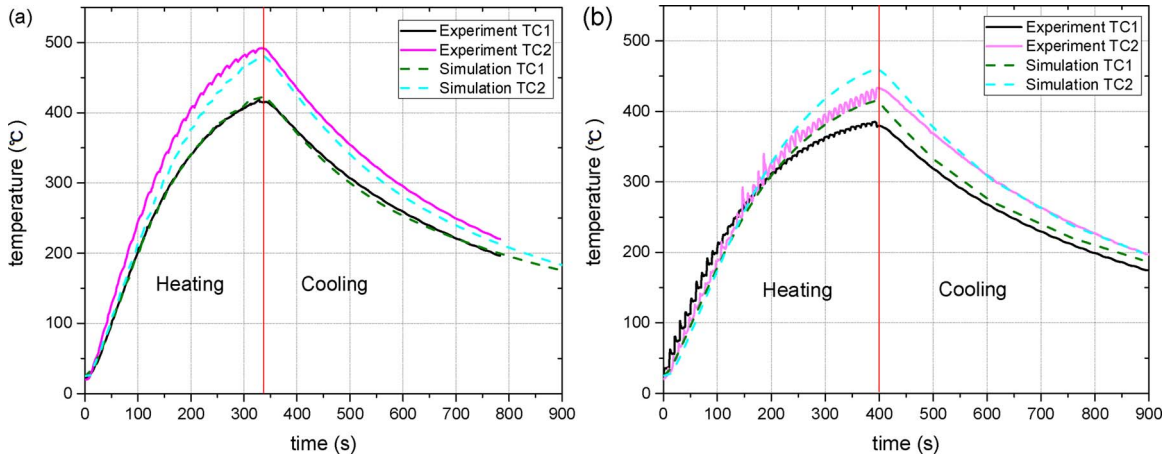

Fig. 8. Comparison between calculated and recored thermal history at each thermocouple according to different scanning strategie: (a) Case 1, (b) Case 2.

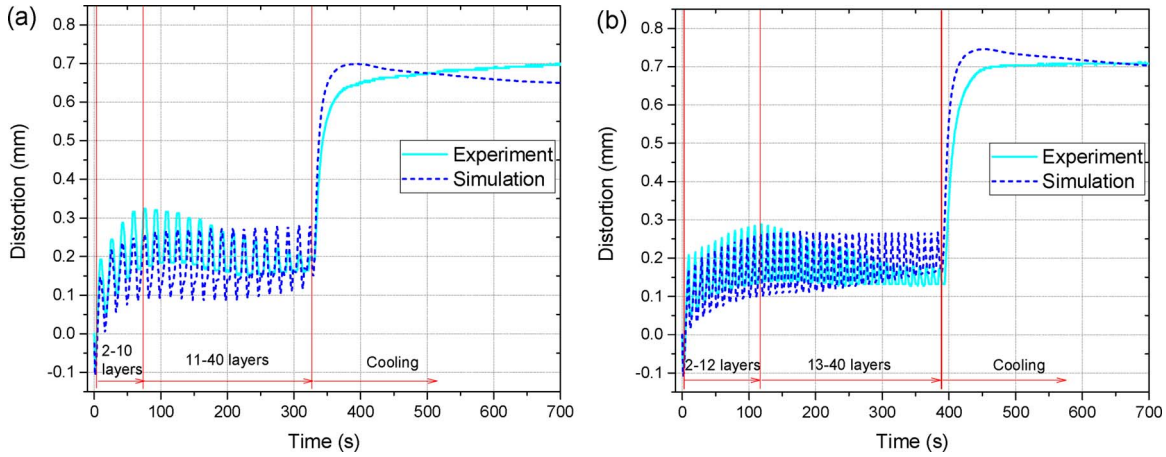

Fig. 9. Comparison between the calculated and measured distortions for different scanning strategies: (a) Case 1; (b) Case 2.

substrate leads to the plate bending and the generation of plastic deformations. This distortion is about −0.1 mm. During the period in which the 2nd to 10th layers are deposited, the distortion of the substrate gradually increases due to the cooling and shrinking of these deposited layers. During the third phase, corresponding to the deposition of all the remaining layers (from 11th to 40th) till completing the built, the distortion of the substrate stabilizes, showing small fluctuations around the same average value. The amplitude of these fluctuations gradually reduces. During the cooling process, the distortion of the substrate sharply increases up to 0.5 mm within 30 s; hence, 70% of the residual distortion develops during the initial part of the cooling phase. Later on, the distortion maintains almost constant.

Fig. 10 shows the temperature field of both the metal deposition and the substrate under Case 1 at the 10th layer deposition. It can be seen that the temperature of the substrate near the metal deposition is higher than 250 °C. The distortion of the substrate and the calculated thermal evolution of point 1 and 2 located at the bottom and edge of substrate respectively are shown in Fig. 11. The power input is continuously transmitted from the metal deposition to the substrate provoking the material softening and, therefore, the plate bending due to the differential thermal expansion. This means that, after the first 10 layers are deposited, the temperature field does not present large temperature gradients responsible of the final distortion. Denlinger [15] found that, when the temperature is close to the alpha-beta phase transformation (600 °C–980 °C), the Ti-6Al-4V alloy undergoes a solid-state transformation. Hence, the annealing process must be accounted for, as well as the gradual reduction of the yield surface. As a consequence, the deformations are mainly due to the plastic flow, so that the actual stress values cannot increase. During the cooling process, the temperature decreases allowing for the material stiffness recovery. As a consequence, most of the distortions take place during this phase. Hence, controlling both the pre-heating temperature and the cooling rate

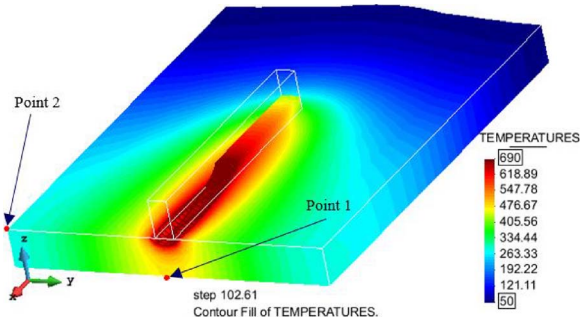

Fig. 10. The temperature field of both the metal deposition and the substrate for Case 1 after 10 layers.

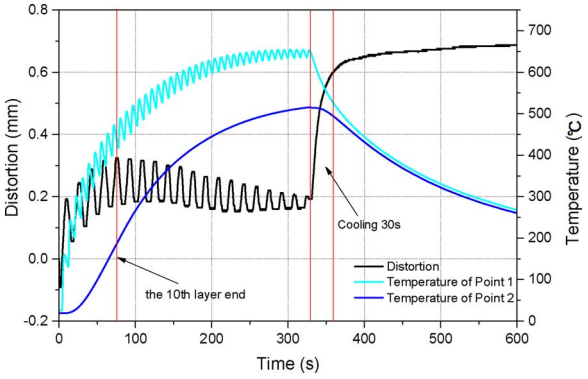

Fig. 11. The evolution of the distortion at the DS position and the calculated temperature evolution at point 1 and point 2, respectively (see Fig. 10).

during the cooling phase is key for the mitigation of residual stresses and distortions.

4.4. Stress field evolution

In this section, the evolution of longitudinal stresses in LSF is discussed using the Case 1 scanning strategy as a reference. Fig. 12 shows the longitudinal stress distributions along the direction of the metal deposition at the mid yz cross-section for different process times. Fig. 12(a) shows variations of the longitudinal stress during the first cladding process. The thermal expansion of the melt-pool (t = 3.78 s) leads to large compressions (−290 MPa) in the material around this zone at the top surface of the substrate. Next, as the melt pool moves (t = 4.0 s), the maximum compressive stresses (−240 MPa) transfer to the HAZ below the melt pool. After that (t = 4.8485 s), the rapid cooling and thermal shrinkage induce large longitudinal tensile stresses (100 MPa) at the top surface of the substrate, leading to the movement of maximum compressive stress field towards the bottom of the substrate. At time (t = 8.179 s), the continuous cooling and shrinkage of the metal deposition results in very high tensile stress values (480 MPa). The variation of the longitudinal stress distribution along the metal deposition direction during the whole AM process is shown in Fig. 12(b). The stress distributions after the deposition of the 1st, 2nd and 5th layer show that the maximum tensile stresses are located in the HAZ at the interface between the metal deposition and the substrate. Moreover, by increasing the number of deposited layers the (compressive) stress field is also consistently increased. The stress distribution produced by the deposition of layers 20th–40th leads to a stable maximum tensile stress value of 150 MPa located in the substrate. The compressive stresses at the lower surface of the substrate become

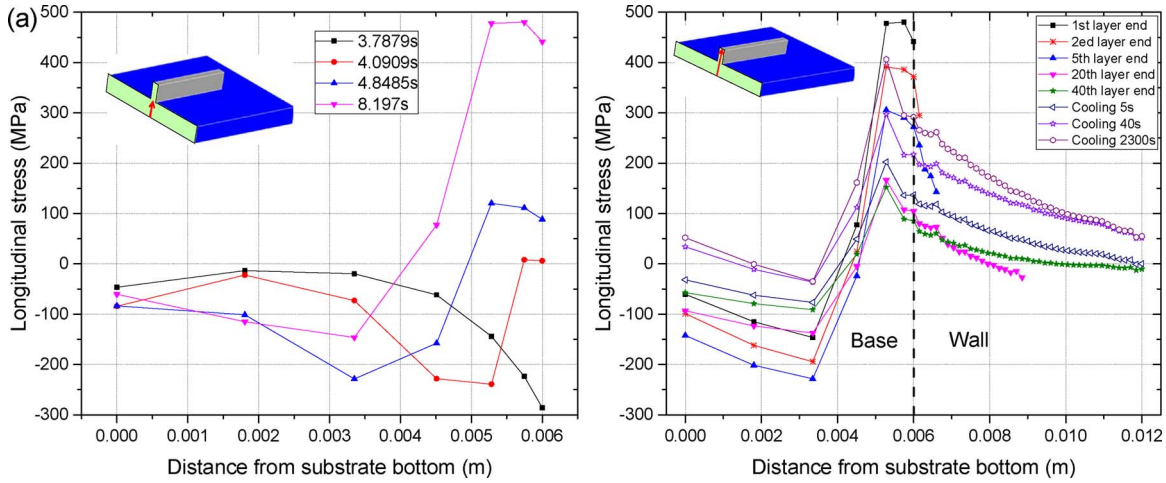

Fig. 12. Calculated stress (σ_{xx}) at the mid yz cross-section for the process: (a) during the 1st layer, (b) at the end of different layers and cooling.

tensile stresses at the top surface. The stress distribution after 5 s, 40 s and 2300 s of the cooling phase shows a sharp overall stress increase (e.g. the maximum tensile stress increases from 150 MPa after the deposition the 40th layer to 410 MPa after 2300 s of the cooling phase, contributing to more than 60% to the maximum residual stress).

Fig. 13 shows the maximum temperature gradients (G_{Zmax}) along the deposition direction according to the metal deposition sequence. It is clear that the maximum temperature gradient and the maximum longitudinal tensile stress occur simultaneously after the deposition of the first layer. They are located in the HAZ of the substrate. According to the continuously metal deposition, the maximum temperature gradient and the maximum stress value gradually reduce and stabilize. These results indicate that large temperature gradients induce large thermal stresses.

The residual longitudinal stresses and von Mises stress distribution at the mid yz cross-section after the deposition of the 40 layers are shown in Figs. 14 and 15, respectively. Observe that the area near the interface between the metal deposition and the substrate exhibits the largest tensile stresses. The maximum tensile stress value appears in the HAZ, just below the upper surface of the substrate (about 1 mm below it). The whole metal deposition shows tensile stresses which gradually reduce along the depositing direction. Although the residual stress distributions obtained using two different scanning strategies are similar, largest residual stresses are obtained when the unidirectional scanning path is adopted. This is because with this scanning strategy the cooling time from layer to layer is larger than using the reciprocating scanning sequence. Hence, the unidirectional scanning path reduces the average temperature distribution while increasing the temperature gradients which provoke the stress formation to both the deposit and substrate.

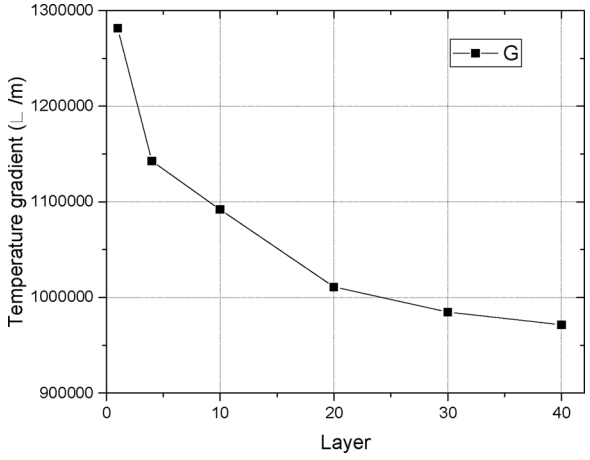

Fig. 13. The maximum temperature gradients (G_{Zmax}) along the deposit direction according to the deposition sequence.

Fig. 16 shows the longitudinal stress distributions along the red line on the upper surface of the substrate (see Fig. 1). The evolution of the longitudinal stress distribution at different times for Case 1 is shown in Fig. 16(a). Observe that the overall longitudinal stresses gradually reduce according to the metal deposition sequence to quickly increase in the final cooling phase. Fig. 16(b) shows the residual longitudinal stress distributions of the upper surface corresponding to both scanning strategies. It can be seen that the stress values at the edges of the metal deposition drastically increases, being about twice of the inside values. This is due to the larger temperature gradients at these locations.

Hence, the deposition of the first layer plays an important role for the formation of thermal stresses because of the colder initial temperature field of the substrate compared to the thermal conditions during the following metal deposition process. By reducing the temperature gradient during the first scanning as well as controlling the cooling rate during the cooling phase is possible to mitigate the development of the distortions and stresses in LSF processes.

5. The influence of pre-heating on distortion and residual stresses

In this section, the influence of pre-heating methods on the development of the final distortions and residual stresses is analyzed. It is well-known that pre-heating the substrate is an effective method to reduce the distortion and residual stresses in AM. However, which method is the most effective remains to be explored. Two kinds of pre-heating methods are here investigated. Firstly, two kinds of scanning patterns applied before the metal deposition are analyzed: (1) longitudinal pattern, in which the laser moves along the longitudinal direction as for the metal deposition; (2) transversal pattern, in which the laser performs the scanning along the direction orthogonal to the metal deposition. Secondly, different pre-heating temperatures applied to the whole substrate are analyzed: 400 °C, 500 °C, 600 °C and 700 °C, respectively.

The results in terms of substrate distortion are shown in Fig. 17. By changing the scanning pattern, the average distortion measured is similar (see Fig. 17(a)). The average distortion of the substrate is about −0.2 mm after pre-heating. Furthermore, it must be observed that at the end of the AM process, the overall distortion of the substrate with pre-heating is higher than without pre-heating. Better results can be achieved by controlling the pre-heating temperature of the whole substrate. In this case, the distortion of the substrate is reduced by increasing the pre-heating temperature to vanish when the value is

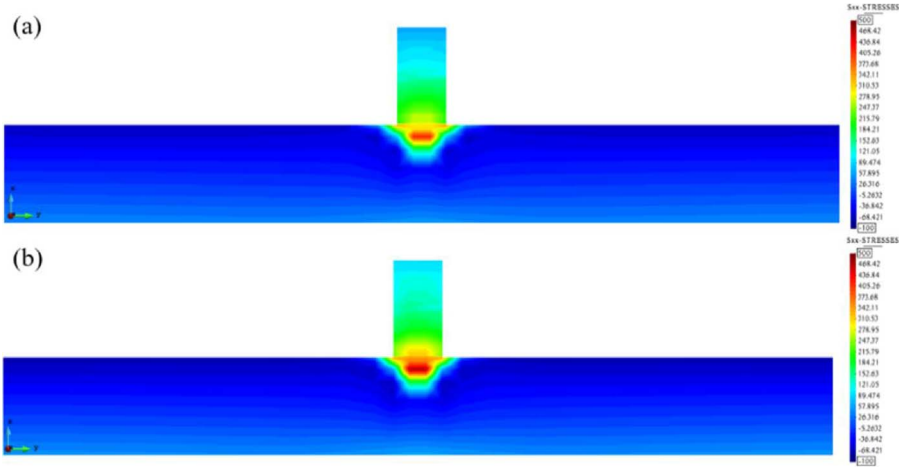

Fig. 14. Calculated residual stresses (σ_{xx}) at the mid yz cross-section: (a) Case 1, (b) Case 2.

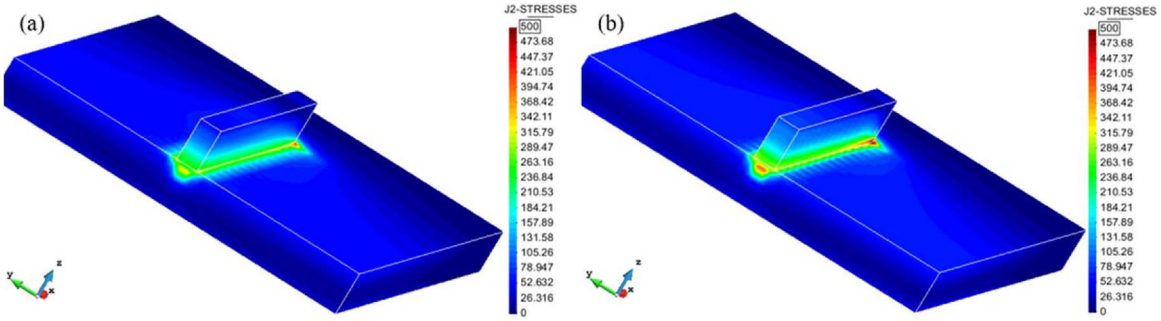

Fig. 15. Calculated residual von Mises stresses at the mid yz cross-section: (a) Case 1, (b) Case 2.

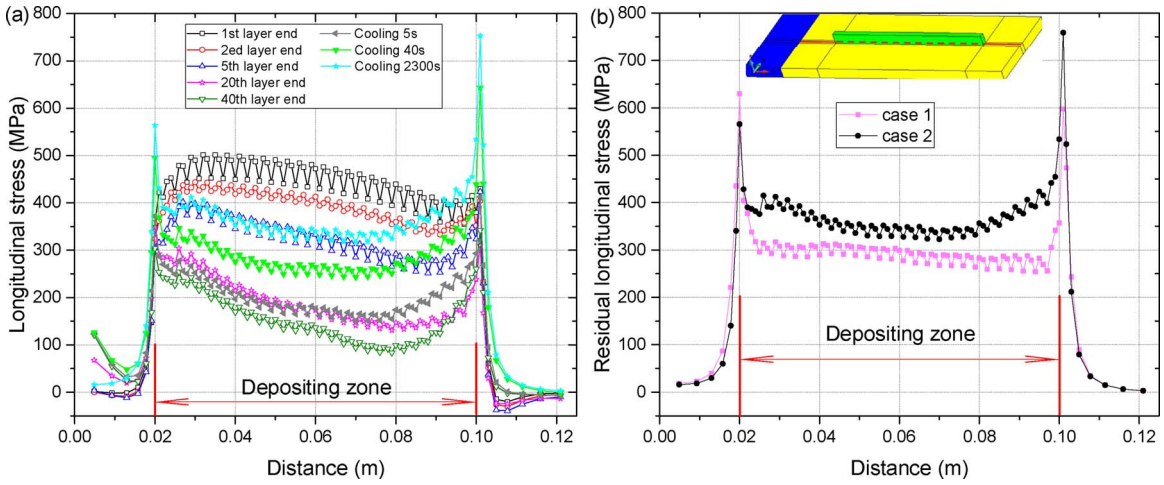

Fig. 16. Calculated stress (σxx) on the upper surface of the substrate: (a) whole process for Case 1; (b) residual stress for both scanning strategies.

around 700 °C. However, the distortion induced in the final cooling phase still exists. This distortion can be alleviated but not removed.

Fig. 18 shows the calculated longitudinal residual stresses according to different pre-heating conditions along the normal direction at the mid yz cross-section. The results show that the pre-heating mitigates the residual stresses while the longitudinal scanning pattern slightly contributes to this mitigation. The longitudinal scanning generates a more uniform temperature field leading to smaller temperature gradients; hence, this is relatively better than the transversal strategy. Focusing on the effect of the pre-heating temperature, the higher is the pre-heating temperature, the smaller are the temperature gradients. So, the maximum residual tensile stresses in both the metal deposition and the substrate are gradually reduced by increasing the pre-heating temperature. When the pre-heating temperature reaches 700 °C, the substrate is fully softened and the maximum residual tensile stresses, located at the top of the metal deposition, does not exceed 50 MPa.

Table 5 shows the reduction of distortion and residual stresses using the different pre-heating strategies used in this work. Similar results have been published by Cao et al. [32] showing that increasing the electron beam pre-heating slightly promotes the mitigation of the maximum residual stress.

6. Conclusion

In this work, a 3D thermo-elasto-visco-plastic finite element model is calibrated and experimentally validated to investigate the

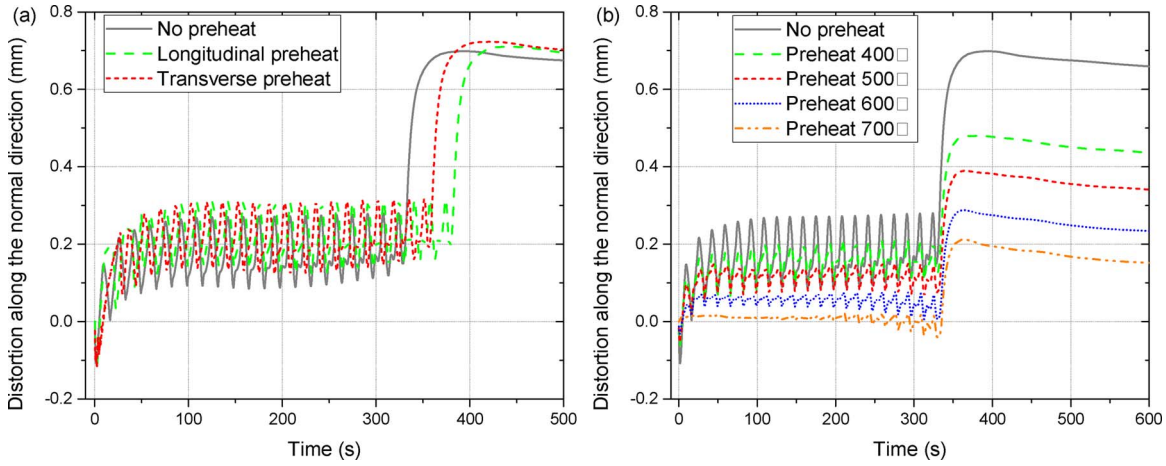

Fig. 17. Plate distortion due to different pre-heating conditions: (a) changing the scanning direction used for the pre-heating; (b) assuming different pre-heating temperatures for the whole substrate.

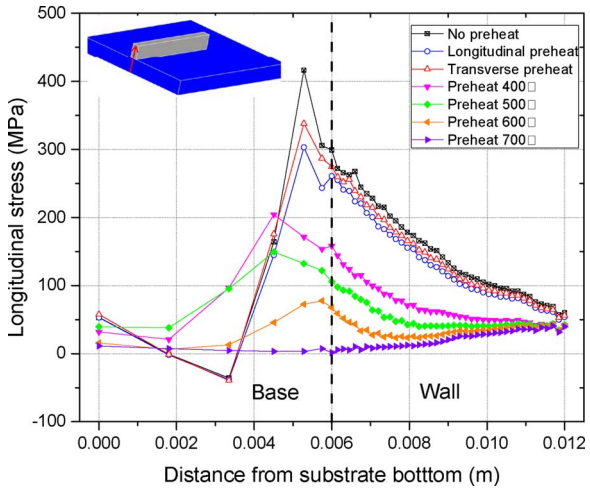

Fig. 18. Calculated residual stress at the mid yz cross-section along the normal direction for different pre-heating conditions.

thermomechanical behavior of LSF technology for the AM process of Ti-6Al-4V. The evolution of both the final distortion and residual stresses under different scanning strategies and the sensitivity to the mechanical properties of Ti-6Al-4V alloy are analyzed. The validated model is used to study the influence of pre-heating on the final distortion and residual stresses induced by the manufacturing process.

The main conclusions are:

1) Different mechanical properties coming from the literature survey for the same Ti-6Al-4V alloy have been tested. The results obtained showed large discrepancies. The most accurate response to correctly characterize the mechanical behavior of the metal deposition in LSF is obtained by adopting the parameters from reference [21]. Hence, for the numerical simulation of the AM process it is mandatory to use material properties which refer to this particular process. Generic material data-base used by other manufacturing processes such as casting or forging are not suitable for AM.

The sensitivity analysis of the mechanical properties of Ti-6Al-4V alloy shows that the distortion and residual stresses strongly depend on the value of the thermal expansion coefficient while slightly depend on the Young's modulus. The influence of the elastic limit is also very significant, because it changes the formation and evolution of the plastic strains.

1) The numerical results are in agreement with the experimental measurements and the maximum average error at the thermocouple TC1 and TC2 is 5.21%.
2) In LSF processes, the maximum temperature gradient and the maximum tensile stress values occur after the deposition of the first layer. This initial stress distribution is not modified by the deposition of the following layers of the built. It is observed that the longitudinal stresses are larger in the HAZ of the substrate and they reduce through the substrate thickness from the bottom to the top surface.
3) The cooling process is the key phase for the development of the residual stresses and distortion: more than 60% of the total amount is generated in this final phase.
4) The scanning strategy adopted for the pre-heating slightly mitigates the residual stresses, while the distortions may increase.
5) Pre-heating the substrate is an effective method to mitigate both the distortion and residual stresses. Increasing the pre-heating temperature, the mitigation is more marked. When the pre-heating temperature reaches 700 °C, the distortion and residual stresses are reduced by 67.2% and 85.1%, respectively.

Acknowledgements

This work was supported by National Natural Science Foundation of China (Nos. 51323008 and 51475380 and 51604227) and the National Key Technologies R & D Program (Nos. 2016YFB1100100 and

Table 5
Reduction of distortion and residual stress for different preheat connditions.

		Longitudinal preheat	Transverse preheat	Preheat 400 °C	Preheat 500 °C	Preheat 600 °C	Preheat 700 °C
Distoetion (%)	Case 1	−2.85	−4.28	35.7	49.5	64.3	75.7
	Case 2	−12.3	−7.53	30.1	41.1	56.2	67.2
Residual stress (%)	Case 1	18.8	27.2	50.9	64.2	81.3	90.4
	Case 2	5.9	14.0	55.4	68.6	83.0	85.1

2016YFB1100602).

Funding from the Spanish Ministry of Economy and Competitivity under the ADaMANT project: *Computational Framework for Additive Manufacturing of Titanium Alloy Components* (ref: DPI2017-85998-P), within the Excellency Programme for Knowledge Generation is gratefully acknowledged.

References

[1] N. Guo, M.C. Leu, Additive manufacturing: technology, applications and research needs, Front. Mech. Eng. 8 (3) (2013) 215–243.
[2] Huang Weidong, Li Yanmin, Feng Liping, et al., Laser solid forming of metal powder materials, Mater. Eng. 3 (2002) 40–43.
[3] L. Qian, J. Mei, J. Liang, et al., Influence of position and laser power on thermal history and microstructure of direct laser fabricated Ti-6Al-4V samples, Mater. Sci. Technol. 21 (5) (2005) 597–605.
[4] S. Kolossov, E. Boillat, R. Glardon, et al., 3D FE simulation for temperature evolution in the selective laser sintering process, Int. J. Mach. Tools Manuf. 44 (2) (2004) 117–123.
[5] P. Peyre, P. Aubry, R. Fabbro, et al., Analytical and numerical modelling of the direct metal deposition laser process, J. Phys. D 41 (2) (2008).
[6] P.M. Sammons, D.A. Bristow, R.G. Landers, Height dependent laser metal deposition process modeling, J. Manuf. Sci. Eng. 135 (5) (2013) 054501.
[7] N. Shen, K. Chou, Thermal modeling of electron beam additive manufacturing process. Powder Sinter. Effects. ASME Paper No. MSEC2012-7253, 2012.
[8] M. Jamshidinia, Numerical modeling of heat distribution in the electron beam melting of Ti-6Al-4V, J. Manuf. Sci. Eng. 135 (6) (2013) 61010–61011.
[9] M. Mughal, H. Fawad, R. Mufti, Three-dimensional finite-element modelling of deformation in weld-based rapid prototyping, Proc. Inst. Mech. Eng. Part C: J. Mech. Eng. Sci. 220 (220) (2006) 875–885.
[10] A. Andrés, V.D. Fachinotti, E. Gustavo, et al., Computational modelling of shaped metal deposition, Int. J. Numer. Methods Eng. 85 (1) (2011) 84–106.
[11] M. Chiumenti, M. Cervera, A. Salmi, et al., Finite element modeling of multi-pass welding and shaped metal deposition processes, Comput. Methods Appl. Mech. Eng. 199 (37–40) (2010) 2343–2359.
[12] S. Marimuthu, D. Clark, J. Allen, et al., Finite element modelling of substrate thermal distortion in direct laser additive manufacture of an aero-engine component, Proc. Inst. Mech. Eng. Part C: J. Mech. Eng. Sci. 227 (9) (2013) 1987–1999.
[13] A. Lundbäck, L.E. Lindgren, Modelling of metal deposition, Finite Elements Anal. Des. 47 (10) (2011) 1169–1177.
[14] A. Plati, J.C. Tan, I.O. Golosnoy, et al., Residual stress generation during laser cladding of steel with a particulate metal matrix composite, Adv. Eng. Mater. 8 (7) (2006) 619–624.
[15] E.R. Denlinger, J.C. Heigel, P. Michaleris, Residual stress and distortion modeling of electron beam direct manufacturing Ti-6Al-4V, Proc. Inst. Mech. Eng. Part B: J. Eng. Manuf. 229 (10) (2015) 1803–1813.
[16] M. Chiumenti, X. Lin, M. Cervera, W. Lei, Y. Zheng, W. Huang, Numerical simulation and experimental calibration of Additive Manufacturing by blown powder technology. Part I: thermal analysis, Rapid Prototyp. J. 23 (2) (2017) 448–463.
[17] J. Yang, S. Sun, M. Brandt, et al., Experimental investigation and 3D finite element prediction of the heat affected zone during laser assisted machining of Ti6Al4V alloy, J. Mater. Process. Technol. 210 (15) (2010) 2215–2222.
[18] E.R. Denlinger, P. Michaleris, Effect of stress relaxation on distortion in additive manufacturing process modeling, Addit. Manuf. 12 (2016) 51–59.
[19] A. Lundbäck, R. Pederson, M.H. Colliander, et al., Modeling and experimental measurement with synchrotron radiation of residual stresses in laser metal deposited Ti-6Al-4V, Proceedings of the 13th World Conference on Titanium, John Wiley & Sons, Inc., 2016, pp. 1279–1282.
[20] X. Zhao, A. Iyer, P. Promoppatum, et al., Numerical modeling of the thermal behavior and residual stress in the direct metal laser sintering process of titanium alloy products, Addit. Manuf. 14 (2017) 126–136.
[21] L. Parry, I.A. Ashcroft, R.D. Wildman, Understanding the effect of laser scan strategy on residual stress in selective laser melting through thermo-mechanical simulation, Addit. Manuf. 12 (2016) 1–15.
[22] M. Chiumenti, M. Cervera, N. Dialami, et al., Numerical modeling of the electron beam welding and its experimental validation, Finite Elem. Anal. Des. 121 (2016) 118–133.
[23] B. Babu, L.E. Lindgren, Dislocation density based model for plastic deformation and globularization of Ti-6Al-4V, Int. J. Plast. 50 (2013) 94–108.
[24] E.R. Denlinger, J.C. Heigel, P. Michaleris, et al., Effect of inter-layer dwell time on distortion and residual stress in additive manufacturing of titanium and nickel alloys, J. Mater. Process. Technol. 215 (2015) 123–131.
[25] F. Martina, M.J. Roy, B.A. Szost, et al., Residual stress of as-deposited and rolled wire+ arc additive manufacturing Ti-6Al-4V components, Mater. Sci. Technol. 32 (14) (2016) 1439–1448.
[26] B.A. Szost, S. Terzi, F. Martina, et al., A comparative study of additive manufacturing techniques: residual stress and microstructural analysis of CLAD and WAAM printed Ti-6Al-4V components, Mater. Des. 89 (2016) 559–567.
[27] K. Weman, Welding Processes Handbook, Elsevier, 2011.
[28] R. Chin, J. Beuth, C. Amon, Control of residual thermal stresses in shape deposition manufacturing, Proceedings of the Solid Freeform Fabrication Symposium, Austin, TX, August, 1995, pp. 221–228.
[29] N.W. Klingbeil, J.L. Beuth, R.K. Chin, et al., Residual stress-induced warping in direct metal solid freeform fabrication, Int. J. Mech. Sci. 44 (1) (2002) 57–77.
[30] J. Cao, M.A. Gharghouri, P. Nash, Finite-element analysis and experimental validation of thermal residual stress and distortion in electron beam additive manufactured Ti-6Al-4V build plates, J. Mater. Process. Technol. 237 (2016) 409–419.
[31] M. Cervera, C. Agelet de Saracibar, M. Chiumenti, COMET: Coupled mechanical and thermal analysis. Data input manual, version 5.0, technical report IT-308, (2002) http://www.cimne.upc.edu.
[32] GiD: the Personal Pre and Post-Processor, CIMNE, Technical University of Catalonia, 2002, http://gid.cimne.upc.edu.
[33] M. Chiumenti, Q. Valverde, C.A. De Saracibar, et al., A stabilized formulation for incompressible elasticity using linear displacement and pressure interpolations, Comput. Methods Appl. Mech. Eng. 191 (46) (2002) 5253–5264.
[34] M. Cervera, M. Chiumenti, C. Agelet de Saracibar, Softening, localization and stabilization: capture of discontinuous solutions in J2 plasticity, Int. J. Numer. Anal. Methods Geomech. 28 (5) (2004) 373–393.
[35] M. Cervera, M. Chiumenti, C.A. de Saracibar, Shear band localization via local J 2 continuum damage mechanics, Comput. Methods Appl. Mech. Eng. 193 (9) (2004) 849–880.
[36] M. Cervera, M. Chiumenti, Q. Valverde, et al., Mixed linear/linear simplicial elements for incompressible elasticity and plasticity, Comput. Methods Appl. Mech. Eng. 192 (49) (2003) 5249–5263.
[37] S.E. Benzley, E. Perry, K. Merkley, et al., A comparison of all hexagonal and all tetrahedral finite element meshes for elastic and elasto-plastic analysis, Proceedings, 4th International Meshing RoundTable Sandia National Laboratories, Albuquerque, NM, 1995, pp. 179–191.
[38] R. Boyer, G. Welsch, E.W. Collings, Materials Properties Handbook: Titanium Alloys, ASM International, 1994, p. 514.
[39] M. Megahed, H.W. Mindt, N. N'Dri, et al., Metal additive-manufacturing process and residual stress modeling, Integr. Mater. Manuf. Innov. 5 (1) (2016) 4.
[40] N. Hoye, H.J. Li, D. Cuiuri, et al., Measurement of residual stresses in titanium aerospace components formed via additive manufacturing, Materials Science Forum vol. 777, Trans Tech Publications, 2014, pp. 124–129.
[41] J. Ding, P.A. Colegrove, J. Mehnen, et al., Thermo-mechanical analysis of wire and arc additive layer manufacturing process on large multi-layer parts, Comput. Mater. Sci. 50 (12) (2011) 3315–3322.
[42] Y.H. Chew, J.H. Pang, G. Bi, et al., Thermo-mechanical model for simulating laser cladding induced residual stresses with single and multiple clad beads, J. Mater. Process. Technol. (2015) 89–101.